Geophysical Journal International

Geophys. J. Int. (2016) **207,** 1513–1528
Advance Access publication 2016 September 25
GJI Seismology

doi: 10.1093/gji/ggw360

Investigating source directivity of moderate earthquakes by multiple approach: the 2013 Matese (southern Italy) $M_w = 5$ event

Vincenzo Convertito,[1] Nicola Alessandro Pino[1] and Francesca Di Luccio[2]

[1] *Istituto Nazionale di Geofisica e Vulcanologia, Osservatorio Vesuviano, Via Diocleziano,* 328, *I*-80124 *Napoli, Italy. E-mail: vincenzo.convertito@ingv.it*
[2] *Istituto Nazionale di Geofisica e Vulcanologia, Via di Vigna Murata,* 605, *I*-00143 *Roma, Italy*

Accepted 2016 September 23. Received 2016 September 21; in original form 2016 March 4

SUMMARY

Preferential direction in rupture propagation of earthquakes is known to have strong consequences on the azimuthal distribution of the ground motion. While source directivity effects are well established for large seismic events, their observation for moderate and small earthquakes are still restricted to a few cases. This is mainly due to intrinsic difficulties in recognizing source directivity unambiguously for less energetic/shorter ruptures. Therefore, we propose the use of multiapproach analysis for revealing the possible directivity for small-to-moderate earthquakes, taking advantage of the different sensitivity of each approach to various source and propagation characteristics. Here, we demonstrate that the application of six diverse and independent methods converges in giving consistent information on the rupture kinematics of the 2013 December 29, $M_w = 5.0$ earthquake. The results indicate a distinct rupture propagation direction toward S-SW, which correlates with observed asymmetry of damage and felt area. Overall, we conclude that the use of a single technique cannot provide a univocal solution, whereas the application of distinct analyses helps to strongly constrain source kinematics and should be preferred, in particular when dealing with small-to-moderate earthquakes.

Key words: Earthquake source observations; Europe.

1 INTRODUCTION

Rupture during an earthquake is commonly thought to initiate in a single point or small patch, then propagating along a fault surface. This may cause distinct asymmetry in the slip distribution with respect to the nucleation point. From the point of view of the shaking at the surface and of the related damage distribution, these features could result in strong azimuthal variations, with dramatic consequences, particularly for large seismic events, in terms of death's toll and building collapse (e.g. Bernard *et al*. 1996; Wald *et al*. 1996; Bouchon *et al*. 2002; Convertito & Pino 2014). However, a number of studies recognized rupture propagation asymmetry for moderate (e.g. Pino & Mazza 2000; Di Luccio & Pino 2011; Holden 2011; Ameri *et al*. 2012; López-Comino *et al*. 2012; Dreger *et al*. 2015) and small (e.g. McGuire 2004; Convertito & Emolo 2012; Kane *et al*. 2013) earthquakes as well, also evidencing correlation of source directivity and felt area extent (e.g. Courboulex *et al*. 2013). Besides these effects, a preferential direction of the rupture propagation may enhance the probability of activation of nearby faults, by means of dynamic triggering (e.g. Gomberg & Bodin 1994; Gomberg *et al*. 2003; van der Elst & Brodsky 2010, Convertito *et al*. 2013). Finally, together with the aftershock distribution, the analyses of source directivity may contribute to constrain the extent and the orientation of the fault associated with the earthquake, allowing the evaluation of the static stress transfer to close seismogenic structures.

In this context, the 2013 December 29 (17:08:43.35 UTC), $M_w = 5.0$, Matese (southern Italy) earthquake represents a paradigmatic example of the characteristics mentioned above. It is the largest of a sequence of about 250 events lasting from late 2013 to early 2014. The whole sequence, recorded by the seismic network managed by the Istituto Nazionale di Geofisica e Vulcanologia (INGV), started on the same day of the main shock with an $M_L = 2.7$ foreshock that occurred at 17:03:25.14 UTC. A second energetic event ($M_L = 4.2$) occurred on 2014 January 20 (07:21:16.48 UTC). Almost all the events are located at 10–20 km depth (http://cnt.rm.ingv.it, last accessed 2015 July 7), with the main shock occurring at the bottom of this range.

The sequence occurred in the interior of the Matese Massif that is a part of the southern Apennines (Italy), an intricate seismotectonic environment (Ferranti *et al*. 2015). In addition, the propagation of the seismic energy is significantly affected by the complex structural setting, due to strong lateral heterogeneities characterizing the transition from the Apennine chain to the Campania plain. Coherently with the kinematic of the area, the main (Fig. 1) and the larger events of the sequence are characterized by normal fault mechanism oriented NW-SE, parallel to the Apennine chain axis (http://cnt.rm.ingv.it/tdmt/, last accessed 2015 July 7). This area has been shaken by several historical destructive earthquakes since the XV century: 1456, $M_w = 7.2$; 1688, $M_w = 7.0$; 1702, $M_w = 6.6$; 1732, $M = 6.6$; 1805, $M_w = 6.8$ (DISS Working Group 2010). More

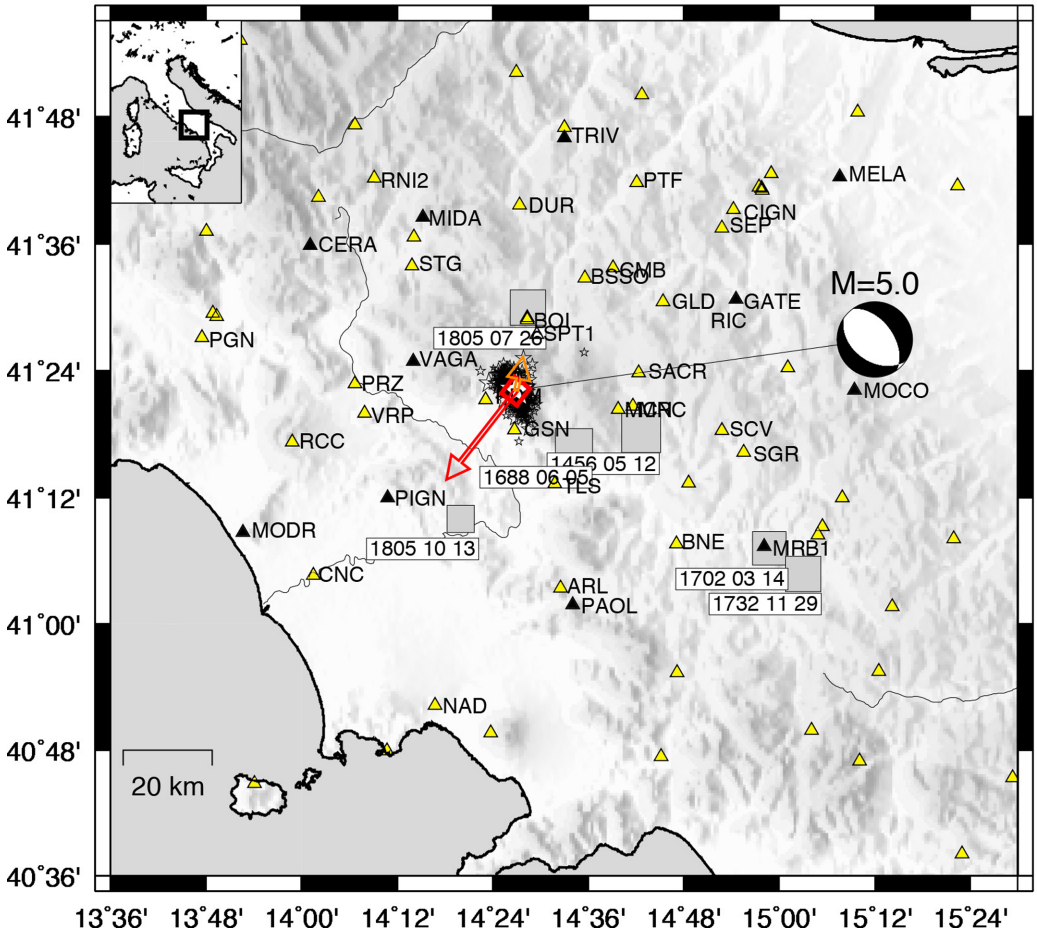

Figure 1. Geographic location of the 2013, $M_w = 5.0$, Matese earthquake (white star) and the aftershocks recorded up to 2014 January 20 (black stars), along with historical earthquakes (grey squares). Yellow and black triangles indicate the recording stations used in our analyses (see the text). The focal mechanism (strike: 125°, dip: 41° and rake: −105°) corresponds to the best double couple of the moment tensor solution retrieved from http://cnt.rm.ingv.it/tdmt. The red arrows identify the SSW dominant (red) and the secondary rupture direction (orange), as resulting from the PGV inversion (Section 2.3.1), while the red box corresponds to the preferred surface fault projection.

recently, light-to-minor magnitude sequences occurred in the same region in 1997–1998 ($M_{max} = 4.2$) and 2001 ($M_{max} = 3.3$)—a few tens of kilometres from the 2013 sequence—whose depth (0–15 km) is shallower than the one described here (Milano *et al.* 2005).

In addition, as reported by Ferranti *et al.* (2015), the 2013–2014 Matese sequence did not involve any of the known faults on which the major historical earthquakes occurred, neither any of those identified by the recent instrumental seismicity, thus indicating the activation of an unknown seismogenic source. Due to the high seismogenic potential of the faults in the region, investigating source directivity is important to infer the possible evolution of the seismic sequence, helping also in the identification of areas where the probability of triggering a nearby event is higher.

Here, we apply six different approaches in order to put as much independent as possible constraints on the source directivity of the Matese $M_w = 5.0$ earthquake. The chosen approaches operate on waveforms features measured in time or frequency domain. In particular, we perform:

(1) Forward and inverse modelling of moment rate functions, derived by means of empirical Green's function (EGF) approach.

(2) Displacement spectral inversion and analyses of the apparent corner frequencies.

(3) Peak ground velocity inversion, by removing propagation and site effect using, respectively, ground motion prediction equations (GMPEs) and EGFs.

Each one of the above techniques is sensitive to specific features of the ground motion (e.g. pulse duration, maximum amplitude and frequency content) that, in turn, contain different information about the seismic source and propagation effects.

2 METHODS AND RESULTS

In all the following analyses, we attempted to derive information on the source kinematics by using the initial assumption of a simple linear horizontal rupture model. We used a simplified version of the directivity function C_d proposed by Ben-Menahem (1961) for a generic bilateral rupture:

$$C_d = \frac{1}{2}\sqrt{\frac{(1+e)^2}{(1-\alpha\cos\vartheta)^2} + \frac{(1-e)^2}{(1+\alpha\cos\vartheta)^2}} \quad (1)$$

where ϑ is the angle between the ray leaving the source and the direction of rupture propagation ϕ (Joyner 1991), and α is the Mach number, that is, the ratio between the rupture velocity v_r (usually assumed closer to *S*-wave velocity) and the velocity c of the considered wave. The larger α the larger the directivity effects, meaning

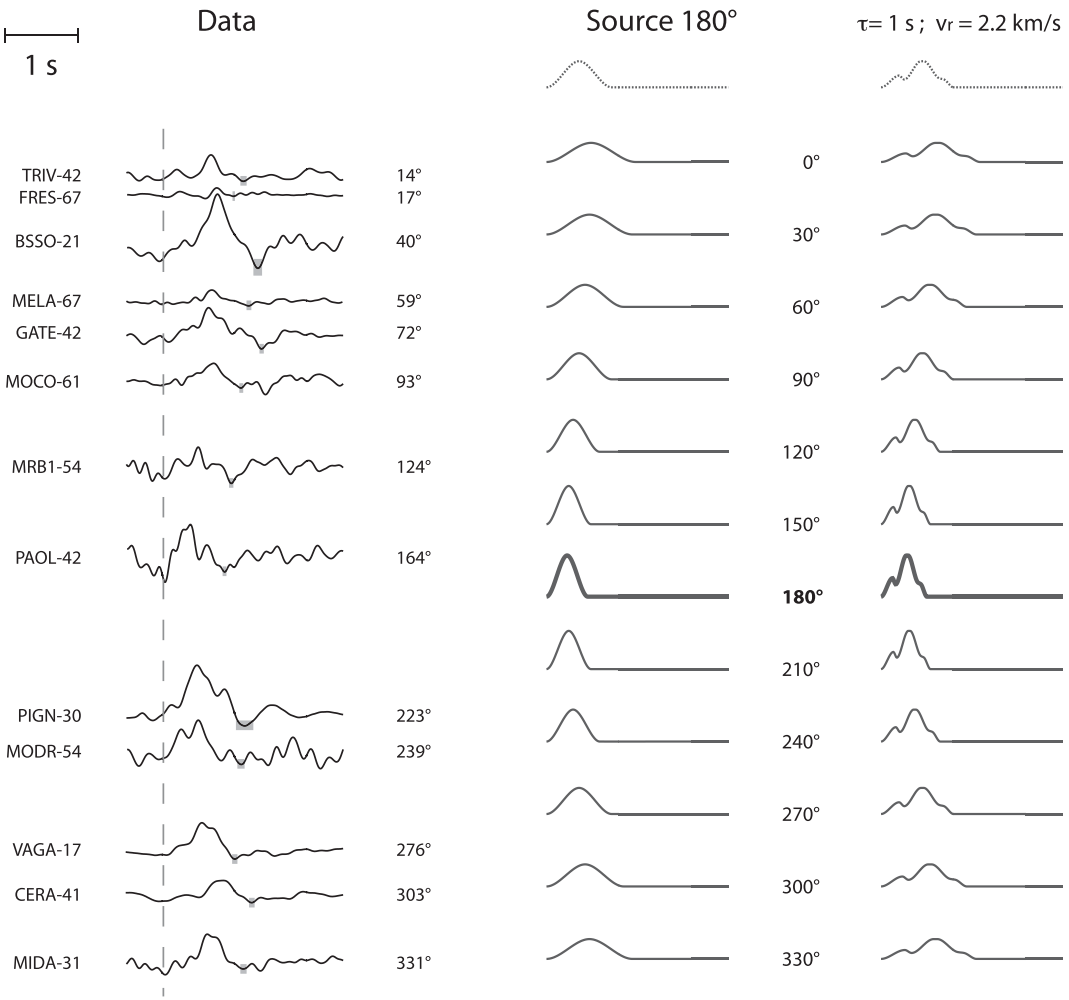

Figure 2. Left: STFs obtained by the deconvolution of the selected EGF. The vertical dashed line corresponds to the time $t = 0$, while the shadowed bands indicate the uncertainty of the end of the STF (see the text). Centre: apparent moment rates predicted, at fixed azimuths, for a source propagating toward N180° at 1.55 km s^{-1} for 1.1 s, displayed on the top of the column. Right: same as centre column, for a different source function, displayed on the top of the column. Each set, data and synthetics, is normalized to the maximum amplitude. Bold traces correspond to the synthetic STFs computed for receiver at 180°, corresponding to the rupture propagation direction.

that variations are expected to be more evident for *S* rather than *P* waves. The percent unilateral rupture *e* parameter is defined as $(2L' - L)/L$, where L is the total rupture length and L' is the length of the dominant rupture (Boatwright 2007): $e = 1$ corresponds to a unilateral rupture, whereas $e = 0$ corresponds to a bilateral rupture. In the original formulation C_d depends also on the vertical take-off angle and the rupture direction angle from vertically down. However, we verified that, considering (i) the source depth (20 km), (ii) the source–receiver distances (Figs 1 and 2) and (iii) the crustal structure ($v_P = 7$ km s^{-1}, at 20 km depth), we could neglect the contribution of the take-off angle i_h in the source directivity function, being very close to 90° and, thus, the relative term $\sin(i_h)$ in the directivity function being close to 1. Specifically, by taking it equal to 1 we introduce a minor error of 10 per cent for stations less than 30 km away, rapidly falling below 5 per cent for distances over 35 km away, where most of the stations used in our analysis are located. Moreover, by assuming a horizontal line source we dropped the dependence on the rupture direction angle from vertically down. Note that we did not hypothesize a horizontal propagating rupture but, according to the model, we aim at resolving the projection of the rupture velocity on the horizontal plane. The vertical component of the rupture velocity can be then determined by projecting the result onto the fault plane, determined independently in other studies.

As for the rupture duration, the variation of the apparent duration with azimuth of the source directivity, t_a, is described by:

$$t_a = \frac{t}{C_d} \tag{2}$$

with t indicating the actual rupture duration. In case of unilateral rupture propagation ($e = 1$ in eq. 1), eq. (2) is:

$$t_a = \frac{L}{v_r C_d} = \frac{L}{v_r}\ (1 - \alpha \cos\vartheta). \tag{3}$$

Concerning the apparent corner frequency f_{c_a}, we used the following equation with general formulation for C_d:

$$f_{c_a} = f_c\, C_d \tag{4}$$

with f_c indicating the actual corner frequency.

Similarly, the azimuthal variation of the ratio between the peak-ground velocity of the main shock (PGV^{Main}) and the PGV^{EGF} of the EGF is modelled by:

$$\frac{PGV^{Main}}{PGV^{EGF}} = kC_d, \tag{5}$$

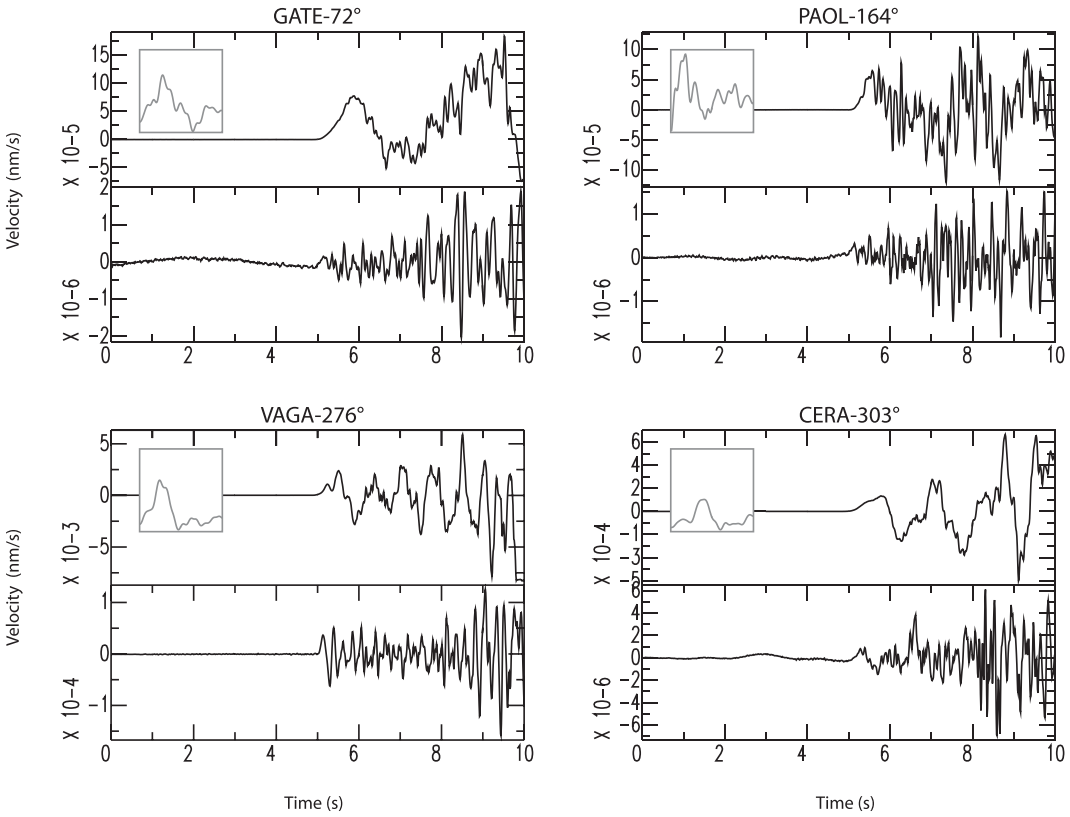

Figure 3. Examples of waveforms for the main shock (top trace) and the EGF (bottom trace). The STF obtained from the deconvolution is shown in the inset. Each panel shows station codes, as indicated in Fig. 1, along with the azimuth of the receiver relative to the source epicentre.

where k is a parameter accounting for the different seismic moment between the two events.

Finally, regarding the peak ground velocity inversion performed by comparing the main shock PGV^{Main} with prediction obtained by means of GMPE, we applied the technique proposed by Convertito *et al*. (2012), which uses the directivity function C_d but in a Bayesian framework.

2.1 Analysis of *P*-wave apparent moment rate function

We determined source kinematics' characteristics through the study of the apparent moment rate functions retrieved at the available seismic stations. We analysed source-time functions (STFs) obtained by means of an EGF approach, where a seismic event, smaller than the investigated one, is considered as a point-like impulsive source. If the hypocentral location and the source mechanism are similar to those of the main shock, the recorded seismograms of the small event would represent the effects of both Earth's structure and source focal mechanism on the main shock recordings. Thus, the deconvolution of the small event recording from that of the large one gives the evolution of seismic moment release with time, as 'seen' at that site, scaled by the seismic moment of the small earthquake.

In order to choose a small earthquake to be used as EGF, we searched among the sequence those events with both long-period, normalized waveforms and location similar to the main shock, but with significantly smaller magnitude. We used the available stations of the Italian National Seismic Network: either broad-band (40 s) or very broad-band (120 s) Trillium sensors. We deconvolved the vertical *P*-wave trains by applying spectrum water levelling at 10 per cent of the maximum spectral amplitude—with no constraints—above 0.2 Hz and up to 6 Hz, well below the EGF corner frequency (∼10 Hz). Due to the moderate maximum magnitude and to the depth of the sequence, and also to the stations' distribution, only few small events could be considered as EGF. We tested the available events by comparing their waveforms with those of the main shock, both low-pass filtered below the corner frequency of the latter. The preferred one is the aftershock that occurred on 2013 December 29, at 20:14:38 UTC, $M_L = 3.2$—with location differing from that of the main shock by less than 2 km horizontally and about 2.5 km in depth—providing the most convincing apparent moment rates. Fig. 2 (left column) shows the results for the 13 stations indicated by black triangles in Fig. 1. Some examples of the main shock and the EGF waveforms are displayed in Fig. 3, along with the relevant STF.

Overall, the resulting apparent moment rates appear to vary with azimuth, exhibiting slightly shorter duration and higher complexity at recording sites located S-SW of the epicentre. On the other hand, the maximum amplitude shows significant differences, even at stations with relatively similar azimuth, likely due to both instability of the deconvolution and possible small differences in location and focal mechanism between the main shock and the EGF. However, except for a couple of stations (BSSO and GATE), the maximum amplitude of the apparent moment rates is clearly lower at northern stations and gradually increases moving to S-SW. These evidences indicate a possible source directivity effects, with southward rupture propagation.

2.1.1 Forward modelling

As a first trial, we attempted to derive information on the source kinematics by using a forward modelling approach, based on the assumption of a simple linear horizontal source model. With the basic

initial hypothesis of unilateral rupture, we computed the apparent duration (t_a) at the available sites according to the directivity eq. (2), with $c = v_P$ the *P*-wave velocity. At each site, the amplitude is scaled by equating the pulse area to the total seismic moment M_0.

Based on the observations described previously, we first considered a simple source pulse and computed synthetic STFs for a rupture propagating toward N180°, embedded in a crust characterized by *P*-wave velocity $v_P = 6.2$ km s^{-1} (interpolated from the 1-D model proposed by Milano *et al*. 2005). In order to define suitable values for L and v_r, we estimated the apparent source duration from the available STFs. We hand-picked the duration of the STFs and assumed the uncertainty as the interval from there to the time corresponding to the 30 per cent of the amplitude measured from the pick to the nearest relative maximum (Fig. 2). Picked durations depend on azimuth and range between 0.85 and 1.35 s, with an average of 1.1 s. At this stage, we simply assumed the latter as the actual rupture time. Accordingly, using $v_P = 6.2$ km s^{-1} in the directivity equation, a rupture velocity of 1.55 km s^{-1} should be considered in eq. (3) in order to justify the observed maximum and minimum apparent duration, which in turn would give rupture length $L = 1.7$ km.

We note that the rupture velocity resulting above is lower than that of other Italian normal fault earthquakes (Pino & Mazza 2000; Pino *et al* 2000, 2008; Di Luccio & Pino 2011) and the rupture length is shorter than what is predicted by Wells & Coppersmith (1994) for an $M \sim 5$ earthquake. This can be interpreted as an indication that a consistent vertical component of the rupture velocity should be considered in addition to the horizontal component accounted in our modelling. On the other hand, the source duration $\tau = 1.1$ s is compatible with what expected for this magnitude (fig. 10 in Kanamori & Brodsky 2004). We remark that this value corresponds to the mean value of the directivity function reproducing the observed source durations, that is, the non-directive duration, and this mean value does not depend on the adopted horizontal rupture model.

Apparently, the predicted variation of the STFs—in duration and amplitude—are significant enough to be detected at the available recording sites and consistent with the evidences described above (Fig. 2, centre column). Then, once the overall variation of the observed apparent moment rates was reproduced satisfactorily, we attempted to use the shape and the relative timing of persistent major waveform inflections as diagnostic elements and attempted to model them. In these regards, despite the relatively short duration of the rupture, we noted the occurrence of a small wiggle preceding the main pulse and the presence of a second minor peak following the main energy release. Both these characteristics are clearly recognizable on all the STFs. Thus, in order to account for these features, we drew a new moment rate function by adding two small wiggles to the synthetic source pulse and computed a new set of moment rate functions. The inflections of the resulting functions are in general agreement with the observed ones (Fig. 2, right column). In particular, the variation of the relative time and amplitude of the small peaks included in the simulation reproduces quite well the arrivals of the corresponding peaks recognizable in the actual STFs. This result evidences the presence of source complexities for the analysed earthquake and confirms the above hypotheses on its rupture propagation. We also tested several combinations of significantly different L and v_r, without getting better results. On the other hand, we did not consider further different moment rate functions, since no other prominent and stable peaks could be identified in the observed STFs.

In order to evaluate the azimuth sensitivity of our results, we computed synthetic STFs for rupture direction of ±30° with respect to the one derived above, keeping L and v_r unchanged (Fig. 4). With respect to the data, the predicted apparent moment rates for

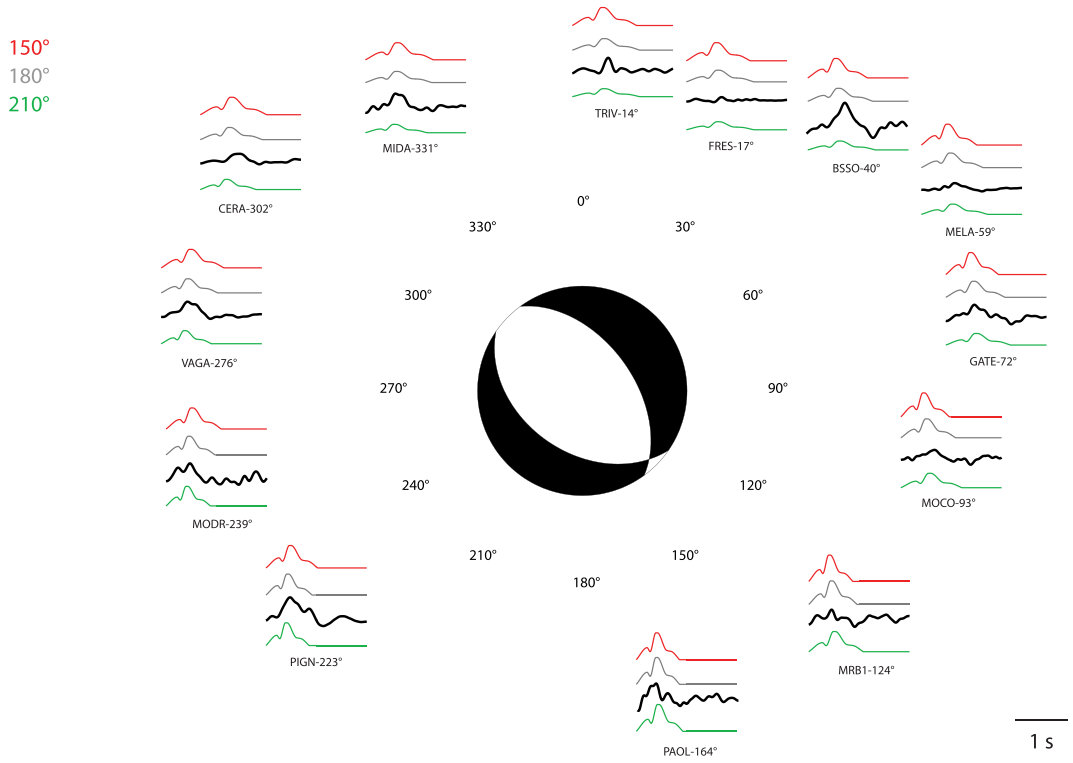

Figure 4. Synthetic STFs obtained for ruptures propagating, respectively, toward N150° (red), N180° (grey) and N210° (green), at $v_r = 1.55$ km s^{-1} for 1.1 s, and observed data (black).

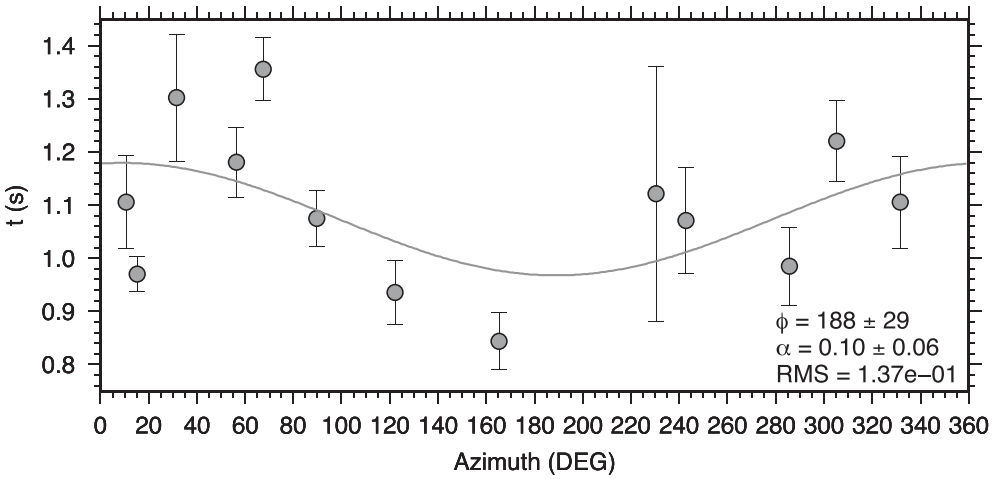

Figure 5. Duration of the STFs illustrated in Fig. 2, as a function of the station azimuth, along with the uncertainty as shown in the same figure. The grey line corresponds to the best fit of data with the directivity function, obtained for the parameters indicated in the bottom right corner (see the text).

rupture propagating toward 150° and 210° produced too short duration at stations located in the eastern and western sectors, respectively, while in the opposite directions such models result in too long sources (due to the quality of the data, at this stage we preferred to evaluate the results through visual comparison. However, as described in the next section, we performed a quantitative analysis of the apparent source duration).

These results indicate that, overall, the 2013 December 29, Matese earthquake occurred on a fault rupturing southward, for 1.1 s, with average velocity $v_r = 1.55$ km s^{-1}. According to our modelling, L and v_r are constrained approximately within ±15 per cent, with a ∼30° uncertainty in the rupture propagation azimuth. We recall that, according to the model assumed above, the inferred length and velocity of the rupture represent the surface projection of the actual values. This could justify the low values obtained for L and v_r.

Finally, we also tested the hypothesis of multiple source pulses, even allowing differential propagation directions, but no significant improvement could be attained to justify the inclusion of further complexity.

2.1.2 Fitting of duration of the source-time functions

As a further check, distinct from the direct modelling of the STF, we inverted the measured apparent durations as a function of the azimuth to determine the rupture propagation direction and velocity for the assumed v_P velocity (Fig. 5). The result clearly indicates a preferential direction toward $\phi = 188° \pm 29°$, with $v_r/v_P = 0.10 \pm 0.06$. This definitely confirms the findings of the STF modelling, but provides with a rupture velocity $v_r \sim 0.62$ km s^{-1} significantly lower than the one used above. We note that the short source duration estimated at TRIV (14°) and FRES (17°) could be a consequence of the low signal-to-noise ratio at these stations, hampering the accurate measurement of the duration. Besides, it should be considered that the filtering of the STFs, aimed at highlighting possible coherent wiggles, lowers the signal-to-noise ratio and has larger effect on the lower amplitude, where the duration is picked, possibly reducing directivity effects.

2.1.3 Inverse modelling

In this study, we implemented an STF inversion technique based on grid search, aimed at retrieving the best rupture direction, the slip distribution, the best rupture velocity and rise time, by assuming a line source model. Specifically, the technique assumes two horizontal line sources of length l_1 and l_2, respectively, originating at the epicentre of the earthquake. Given the magnitude, the whole length $L = l_1 + l_2$ is estimated by using the relationship proposed by Wells & Coppersmith (1994). Using two lines would allow to model rupture processes that do not propagate along a unique dominant direction but may develop in a more complex way. Each line is discretized at a regular step *dl* (subsources), which depends on the rupture velocity and the selected rise time. We allowed the rise time to vary in an interval centred on the value resulting from the empirical relationship provided by Somerville *et al*. (1999).

A triangular source-time function is associated with each subsource *dl*, whose final slip value is randomly extracted from *a-priori* fixed range, based on the event magnitude. The slip on both ends of each line is tapered to avoid unrealistic stopping phases and the total radiated seismic moment is checked against the actual one. Each subsource can slip once and is activated when reached by the rupture front, which propagates from a single nucleation point at a constant rupture velocity v_r. While the first segment is activated at $T = 0$ s, the second one is activated at a time that is randomly chosen in a time interval ranging between 0 and the duration of the first segment, that is, l_1/v_r. Finally, all the elementary sources are summed-up at each station and the obtained synthetic signal is compared with the observed STFs.

Given the data vector $\boldsymbol{d}$ whose components d_i are the observed STFs, we infer the best model $\boldsymbol{x}$, whose components x_i are rupture directions, slip distribution, rupture velocity and rise time, by maximizing the likelihood function LK($\boldsymbol{x}|\boldsymbol{d}$) given by:

$$\mathrm{LK}\ (\boldsymbol{x}|\boldsymbol{d}) = f_1\,(d_1|\boldsymbol{x}) \cdot f_2\,(d_2|\boldsymbol{x}) \ldots f_m\,(d_m|\boldsymbol{x})\,, \tag{6}$$

where $f_i(d_i/\boldsymbol{x})$ is a probability density that allows to compute the probability of observing data in some range for a given model $\boldsymbol{x}$. Assuming that data errors are independent and normally distributed with expected zero value and standard error σ_i, the ith probability density function (pdf) $f_i(d_i/\boldsymbol{x})$ assumes the form:

$$f_i\,(d_i|\boldsymbol{x}) = \frac{1}{(2\pi)^{1/2}\sigma_i}\, e^{-\frac{\{d_i - [G(x)]_i\}^2}{2\sigma_i^2}}\,, \tag{7}$$

where $G(\boldsymbol{x})$ represents the predicted STF (Aster *et al*. 2005). The likelihood function $\mathrm{LK}(\boldsymbol{x}|\boldsymbol{d})$ for the observed data set is thus given by:

$$\mathrm{LK}\left(\boldsymbol{x}|\boldsymbol{d}\right) = \frac{1}{(2\pi)^{m/2}\prod_{i=1}^{m}\sigma_i}\prod_{i=1}^{m} e^{-\frac{\{d_i-[G(x)]_i\}^2}{2\sigma_i^2}}, \tag{8}$$

where m is the product of the number of stations Ns by the number of data points NP in the observed STF. In practice, since the logarithm is a monotonic function, we maximized the logarithm of $\mathrm{LK}(\boldsymbol{x}|\boldsymbol{d})$ arbitrarily assuming a unitary standard error σ_i. We explored rupture velocity values in the range 1.5–3.5 km s^{-1} (uniform steps of 0.1 km s^{-1}), rise time values in the range 0.05–0.3 s (uniform steps of 0.01 s), slip values randomly chosen in the range 0.0–0.5 m, while the direction of both lines varies independently between 0° and 360° (uniform steps of 5°).

As for the uncertainty, we estimated the 95 per cent confidence region using the observed Fisher information matrix $\boldsymbol{I(x)}$

$$\boldsymbol{I}\left(\boldsymbol{x}_{\mathrm{ML}}\right) = -\frac{\partial^2}{\partial x_i \partial x_j}\ln\mathrm{LK}\left(\boldsymbol{x}_{\mathrm{ML}}|\boldsymbol{d}\right) \tag{9}$$

evaluated at the maximum likelihood estimates $\boldsymbol{x}_{\mathrm{ML}}$, and the fact that the inverse of $\boldsymbol{I}(\boldsymbol{x})$ is an estimator of the approximate covariance matrix (Pawitan 2013)

$$\mathrm{Var}\left(\boldsymbol{x}_{\mathrm{ML}}\right) = \left[\boldsymbol{I}\left(\boldsymbol{x}_{\mathrm{ML}}\right)\right]^{-1}. \tag{10}$$

The standard errors are the square roots of the diagonal elements of the covariance matrix and the 95 per cent confidence region for each inverted parameter m_{i} is defined as:

$$x_{i,\mathrm{ML}} \pm \mathrm{crit}\cdot\sqrt{\left[\boldsymbol{I}\left(x_{i,\mathrm{ML}}\right)\right]^{-1}}, \tag{11}$$

where crit is the critical value of the χ^2 distribution with a number of degree of freedom equal to the number of inverted parameters n_{par} (Pawitan 2013).

For the 2013 December 29, Matese earthquake analysed in this study, we used the STFs shown in Fig. 2 (except for FRES and BSSO, displaying unreliable amplitude), resampled at 0.1 s. In order to have positive apparent moment rate functions, for each resampled STF we subtracted its value at $t = 0$ and assumed the end at the first zero crossing. Then, we multiplied the resulting functions by the seismic moment of the EGF. We first assumed two-line sources of length l_1 and l_2 that are, respectively, equal to 50 per cent of the length $L \sim 3$ km, as estimated using the Wells & Coppersmith (1994) relationship. The result of the inversion indicates that the two-line sources rupture at $v_{\mathrm{r}} = 1.8$ (1.6, 1.9) and have azimuth 130° (127, 132) and 250° (245, 255), respectively, producing a log maximum likelihood value of $\mathrm{MLE}_{\mathrm{S2}} = -1643$. The interval in parenthesis corresponds to the 95 per cent confidence interval using crit = 12.6 for $n_{\mathrm{par}} = 6$.

Next, in order to refine the results, we used a single-line source and tested the degree of fitting with respect to the case of two-line sources. Fig. 6 reports the inferred slip distribution and the comparison between the observed and the simulated STFs. The best model, which corresponds to a log maximum likelihood value of $\mathrm{MLE}_{\mathrm{S1}} = -926$, indicates a 185° (172, 198) rupture direction where the 95 per cent confidence interval are computed using crit = 11, for $n_{\mathrm{par}} = 4$. The inferred rise time and rupture velocity are 0.13 (0.08, 0.17) s and 1.8 (1.7, 2.0) km s^{-1}, respectively.

Based on the Akaike information criterion (AIC; Akaike 1974) that relates the number of inverted parameters n_{par} with the logarithm of the maximum likelihood function $\mathrm{LK}(\boldsymbol{x}|\boldsymbol{d})$ through the relation $\mathrm{AIC} = 2n_{\mathrm{par}} - 2\ln\mathrm{LK}(\boldsymbol{x}|\boldsymbol{d})$, the model with a single-line source should be preferred since it corresponds to a lower AIC value. Incidentally, we note that the best direction of the rupture propagation resulting from the single-line source lies right in between the directions obtained for the two-line source.

Finally, assuming the single-line model as the preferred one obtained from the STFs inversion, using again 6.2 km s^{-1} as the v_{P} at 20 km depth (Milano *et al*. 2005) and assuming a $v_{\mathrm{P}}/v_{\mathrm{S}}$ ratio of 1.73, we obtain $v_{\mathrm{S}} = 3.6$ km s^{-1} and a Mach number $\alpha = v_{\mathrm{r}}/v_{\mathrm{S}} = 0.5 \pm 0.2$.

2.2 Spectral inversion and source directivity from corner frequencies

We inverted displacement source spectra in the frequency range 0.03–10.0 Hz. The initial number of waveforms is 126, which were recorded at 42 stations of the Rete Accelerometrica Nazionale (RAN, Dipartimento della Protezione Civile) and Rete Sismica Nazionale (RSN, INGV). Discarding the clipped signals and those affected by very high noise level, we ended up with waveforms from 34 stations (Fig. 1). Accelerograms from RAN are integrated to obtain velocities, while waveforms from RSN are only corrected by the instrument transfer function, which includes both sensor and data-logger responses.

We filtered all the waveforms in the frequency band 0.01–15 Hz and applied a time windowing depending on the hypocentral distance, cutting from 2 s before the manual S wave picking up to 2 s before the expected surface waves arrival time. We applied a 5 per cent cosine taper function and zero padding before computing the Fourier amplitude spectra. Then, the spectra were smoothed by applying an average moving window with a four-point half width. Finally, the S-wave displacement spectra were computed from the modulus of the three components velocity spectra by dividing the spectra by 2π.

All the displacement spectra had a signal-to-noise ratio (in log scale) higher than 3 in the considered frequency band and were corrected by the stations transfer function to account for the site effect. Each station transfer function was obtained as the spectral ratio between horizontal and vertical components by using 251 aftershocks recorded up to 2014 January 20. We are aware that empirical site transfer functions derived through H/V spectral ratio could be affected by amplification on the vertical component or by waves propagating in almost the vertical direction (Parolai *et al*. 2004). Nevertheless, for the available common stations, we compared our functions with those derived by Pacor *et al*. (2016a) by using the generalized inversion technique (GIT), not suffering from these limitations, and verified that our results are compatible with the GIT site transfer functions.

No aftershock waveforms were available at the RAN stations, thus we computed the transfer function by using the main shock waveforms only. Since this approach could produce not well-constrained transfer function, we checked the reliability by repeating this computation at stations where the transfer functions were obtained by means of the available aftershocks, verifying the full correspondence of the functions (Fig. 7).

We assumed the following source model,

$$S\left(f\right) = \frac{\Omega_0}{\left[1+\left(\frac{f}{f_c}\right)^{\gamma n}\right]^{\frac{1}{\gamma}}}, \tag{12}$$

where Ω_0 is the long-period spectral amplitude, f the frequency, f_{c} the corner frequency, n the high-frequency fall-off rate and γ is a

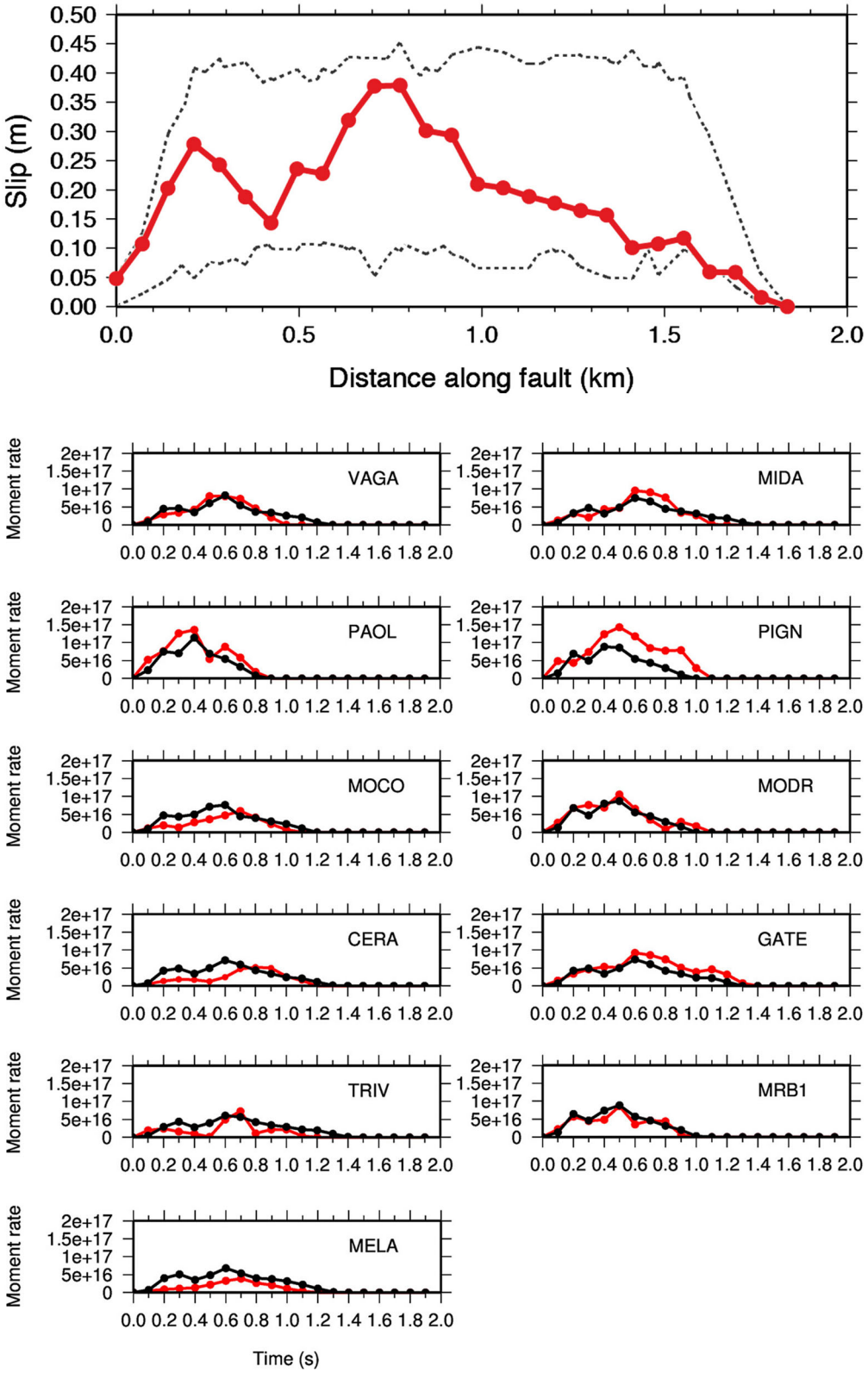

Figure 6. Result of the source-time function inversion. Upper panel shows the final slip distribution corresponding to the best model. Lower panels display the comparison between the observed (red) and predicted (black) apparent moment rate functions at the stations indicated in each panel (see Fig. 1 for locations). Moment rate unit is Nm s^{-1}.

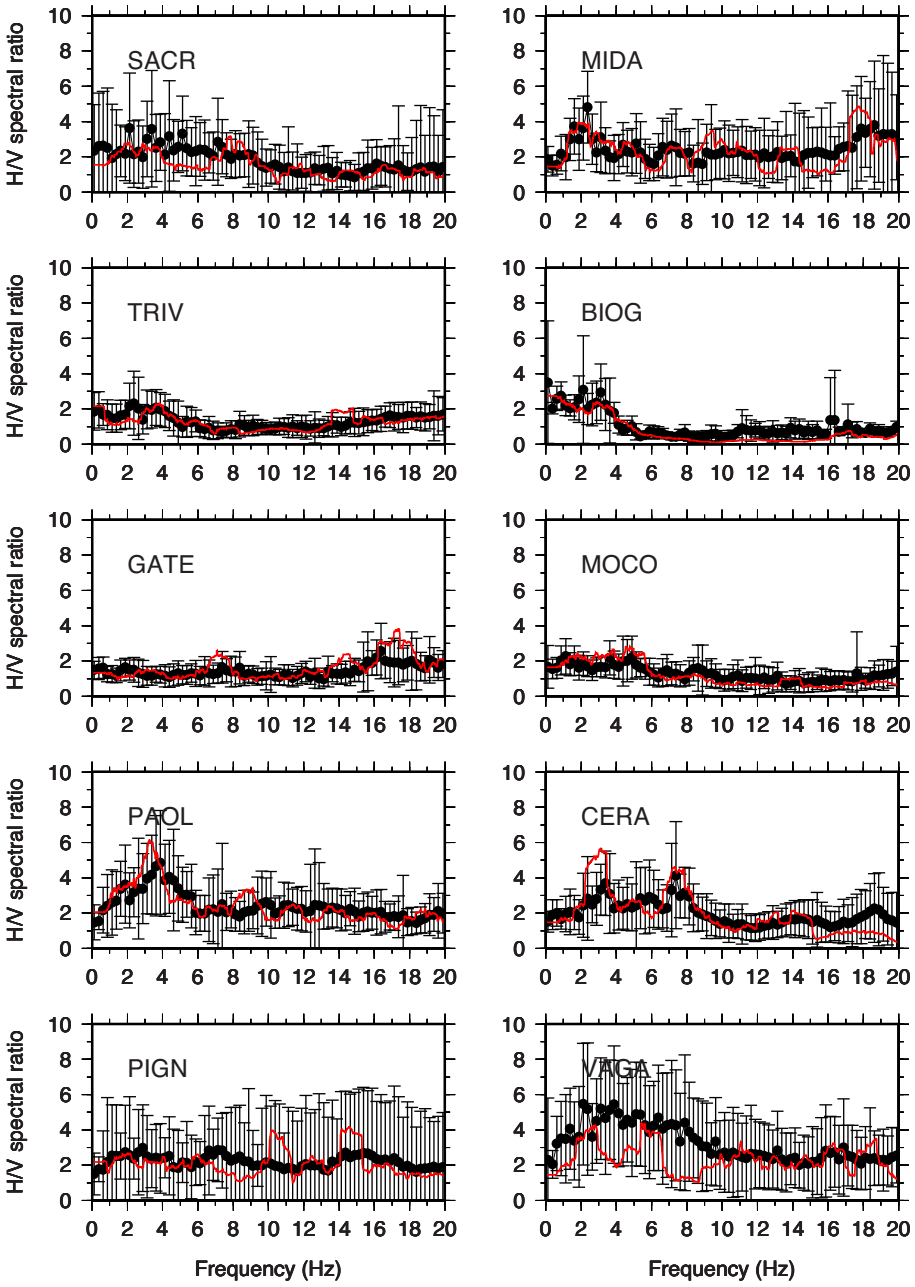

Figure 7. Examples of site response function for 10 stations, as labelled in the upper left corner of each plot (see Fig. 1 for locations), as obtained from the *H*/*V* spectral ratios analysis of 251 aftershocks recorded up to 2014 January 20, shown as mean (black curve) and uncertainty (error bars). Red curves correspond to the *H*/*V* spectral ratios obtained from the analysis of the main shock waveforms.

constant (Boatwright 1980). As for the attenuation, we assumed the following filter,

$$Q(f) = e^{-\pi f \frac{T}{Q_0}}, \tag{13}$$

where Q_0 is the frequency independent quality factor and T is the *S*-wave traveltime. The product of $S(f) \times Q(f)$ provides with the final model to be inverted. We estimated the parameters Ω_0, f_c, n and Q_0, by using the Downhill–Simplex approach (Nelder & Mead 1965). Since there is an intrinsic correlation among some of the parameters (e.g. Sonley & Abercrombie 2006; Zollo *et al*. 2014), it is necessary to implement a strategy to reduce the correlation. To this aim, we iteratively constrained the range of a specific parameter based on the results of each inversion, as described here below. We set $\gamma = 1$ in eq. (12) and selected initial range of exploration for $n = (1, 3)$ and $Q_0 = (50, 1000)$. Next, we re-iterated the inversion procedure by reducing the range of exploration, according to the following scheme:

(1) The n parameter is set to 2, while Q_0 is explored in the range (50, 1000) and is inverted for each station.

(2) For each station, Q_0 is set to the best value obtained from point 1, while n is explored in the range (1.5, 3).

(3) Based on the results obtained from point 2, the range of exploration for n is now restricted, while Q_0 is allowed to vary.

(4) Using the values obtained from point 3, both the range of variation for n and Q_0 are restricted, respectively, to 2.1−2.6 and 450−800 and the final best model is selected.

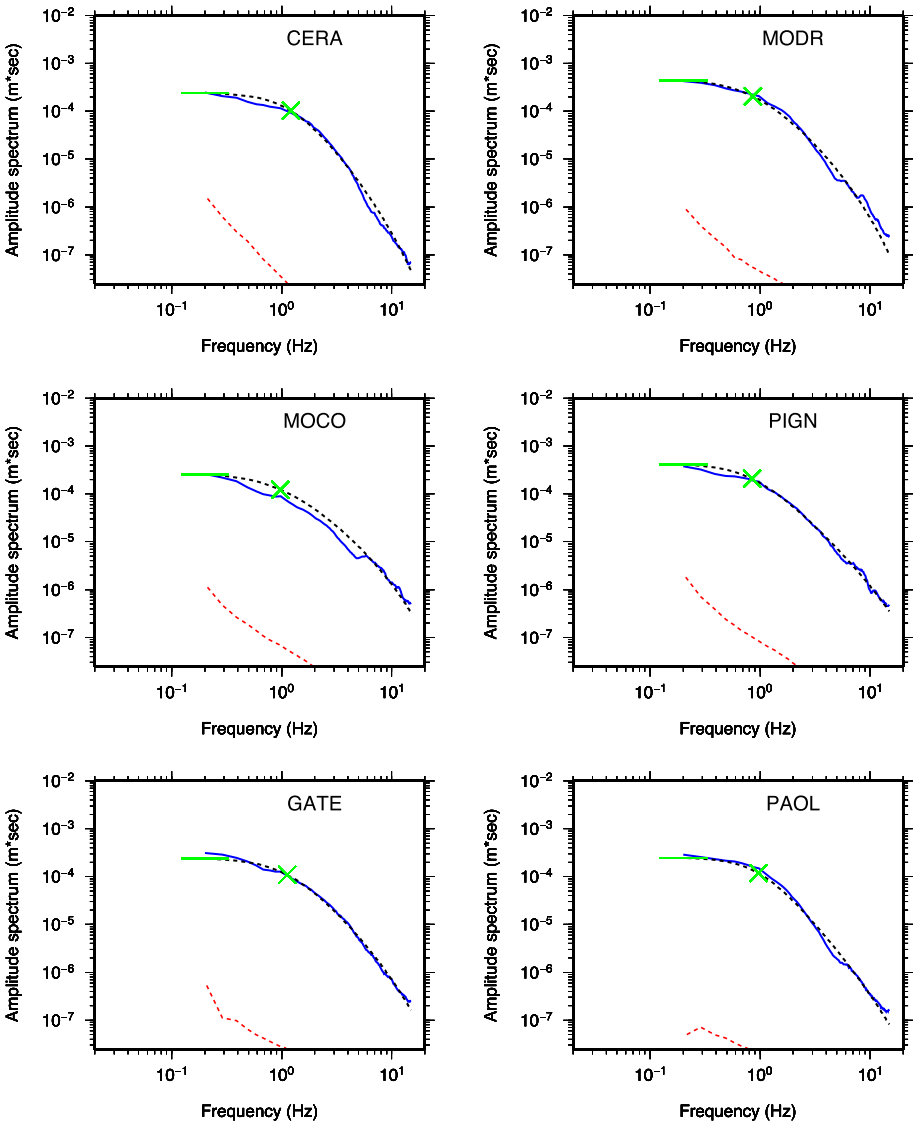

Figure 8. Example of *S*-wave smoothed displacement spectral fitting at six stations, as labelled in the upper right corner of each plot (see Fig. 1 for stations' location). In each panel, the blue curve represents the observed *S*-wave displacement spectrum, the black dashed line is the fitted spectrum whose best parameters are indicated with the green horizontal line (low-frequency spectral level) and the green cross (corner frequency). The red dashed line represents the spectrum of the pre-*P* noise as measured from the waveform.

Fig. 8 shows the observed displacement spectra together with those obtained from the inversion and the noise spectra at six stations (Fig. 1). In order to verify that the implemented inversion technique is finally able to remove possible dependence of both n and Q_0 on the azimuth and distance, for each station we show in Fig. 9 their final values as a function of azimuth and epicentral distance. Notably, the final value of n is 2.4 ± 0.2, slightly larger than the expected value for the ω-square source model (Brune 1970), while the final value of Q_0 is 616 ± 128, compatible with the estimates of intrinsic attenuation in the frequency range 1–12 Hz, provided by Bianco *et al*. (2002) for the southern Apennines.

At each station i, the inferred Ω_0 value is used to compute seismic moment using the following formulation (Aki & Richards 1980),

$$M_o^i = \frac{4\pi\rho_s^{1/2}\rho_r^{1/2}c_s^{5/2}c_r^{1/2}R'\,\Omega_o^i}{F\,R_{\theta\varphi}}\,, \qquad (14)$$

where R' is the geometrical spreading estimated according to Ben-Menahem & Singh (1981), ρ_s and ρ_r are the density at the source and at the receiver, assumed here, respectively, 2800 and 2600 kg m^{-3}; c_s and c_r are the *S*-wave velocities at the source and receiver, here assumed to be 3.9 and 2.6 km s^{-1}, respectively. $R_{\theta\varphi}$ is the average *S*-wave radiation pattern assumed to be 0.7 and F is the free-surface coefficient (fixed to 2).

The obtained seismic moment value M_o is (4.1 ± 0.1) × 10^{16} N m, which corresponds to $M_w \sim 5.0$. This value results from the geometrical mean of Ω_o^i, whereas the uncertainty corresponds to the standard deviation. Assuming a line-source model, the inferred f_{c_a} distribution versus azimuth (eq. 4), reported in Fig. 10, is used to estimate the best parameters of the C_d function. We used the non-linear Levenberg–Marquardt least-squares algorithm (Marquardt 1963) to fit C_d. The inferred best model (Fig. 10) indicates a dominant rupture direction at an azimuth of 169° ± 7°, a unilateral percentage value $e = 0.0 \pm 0.1$ and a Mach number $\alpha = 0.5 \pm 0.1$ (the uncertainties

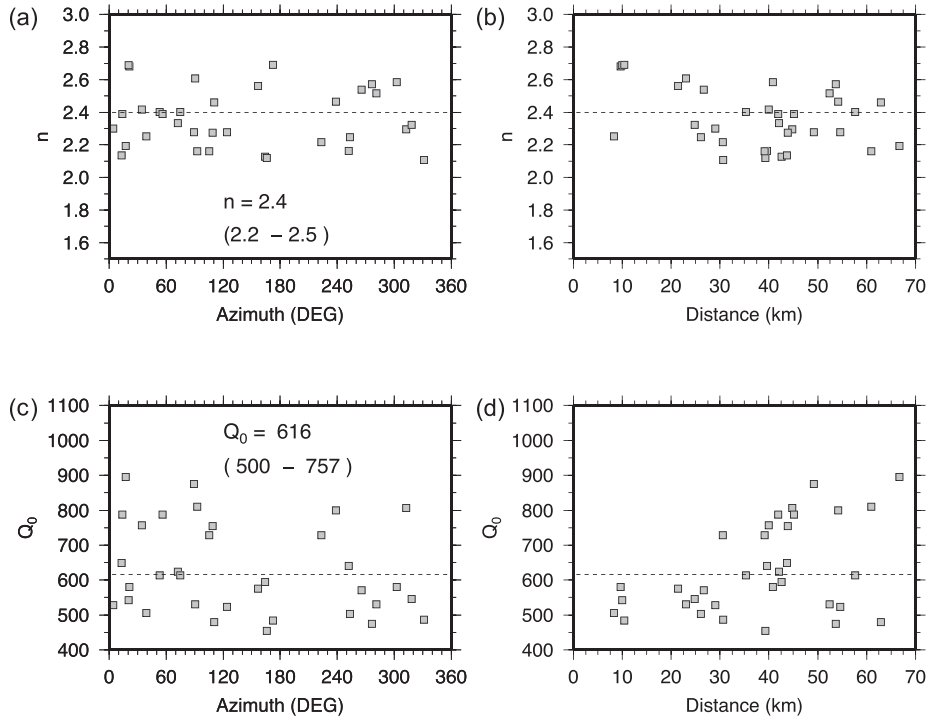

Figure 9. (a) and (c) Distribution of the n-values and Q_0-values as a function of the station azimuth and (b) and (d) the hypocentral distance, respectively. (a) and (c) The mean value of n and Q_0, together with the uncertainty ($\pm 1\sigma$), are reported.

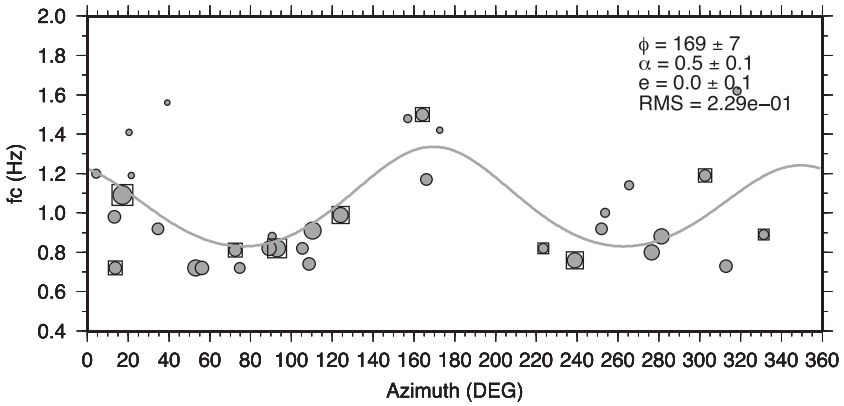

Figure 10. Apparent corner frequency distribution as a function of station azimuth. Grey continuous line represents the best-fit model whose parameters are reported in the upper right corner. Symbol size is proportional to the source-to-station distance. Squares indicate the stations at which STF duration is available (Fig. 5).

correspond to the asymptotic standard errors as given by GNUPLOT; Janert 2009).

2.3 Peak ground velocity inversion

2.3.1 $PGV^{observed}/PGV^{predicted}$

We analysed peak ground velocities (PGVs) as a function of the azimuth to infer surface fault projection and dominant horizontal rupture direction of the investigated earthquake. In particular, we applied a technique that minimizes the difference between observed and predicted PGV values using a grid-searching scheme in a Bayesian framework (Convertito *et al*. 2012). The best model (surface fault projection, ϕ and e) is the maximum *a-posteriori* model (i.e. the model corresponding to the largest value of the *a-posteriori* joint pdf), whereas the uncertainties are retrieved from the analysis of the *a-posteriori* marginal pdfs. In particular, for each parameter, the uncertainty corresponds to the half-width at half-maximum of the marginal pdf.

For the application presented in this study, we used the GMPE proposed by Bindi *et al*. (2011) to produce predictions by using the R_{JB} distance (i.e. the minimum distance of a site from the surface fault projection) metric (Joyner & Boore 1981). In order to account for site effect in the predictions, we associated at each station the average shear wave velocity over the uppermost 30 m (VS_{30}). The VS_{30} values have been extracted from the database compiled for implementing ShakeMap in Italy (Michelini *et al*. 2008). Predictions including site effect are then modified to account for the source directivity through the directivity function C_d (eq. 1).

According to the magnitude of the earthquake, we set the maximum epicentral distance at 150 km and discarded observed PGVs that exceed median prediction more than 2σ (σ being the total

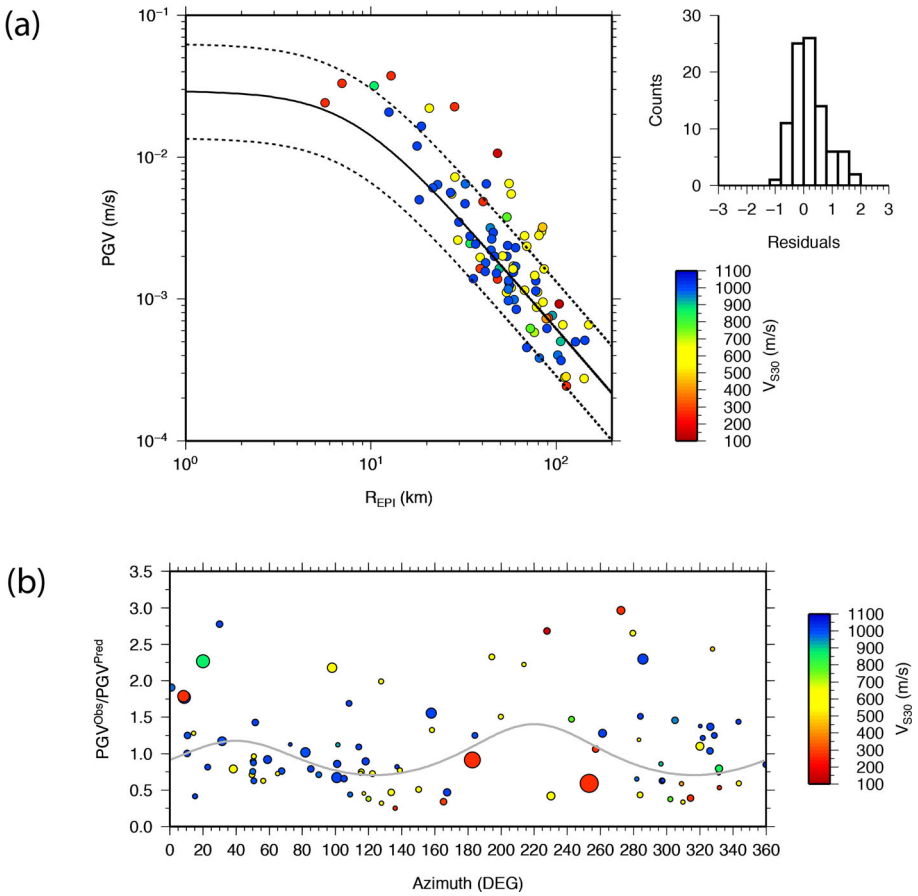

Figure 11. (a) PGV as a function of the epicentral distance. Dots are colour coded according to the VS_{30} value used to modify the prediction. Continuous black line corresponds to the GMPE by Bindi *et al*. (2011), whereas dashed lines correspond to $\pm$ 1σ. The residuals' (i.e. log of the observed minus log of predicted values including VS_{30}) distribution is reported in the upper right corner. (b) Ratio between observed PGV and corresponding values predicted by the GMPE (modified for the VS_{30}), as a function of the station azimuth. Symbol size is proportional to the epicentral distance. The same colour code as (a) is used for VS_{30}. The grey curve is obtained by using the best-model parameters inferred by the PGV inversion (see the text and Fig. 12).

standard error of the GMPE used for the prediction). Differences larger than 2σ might be ascribed to effects that cannot be modelled by the adopted procedure. We obtained a final number of 91 usable stations for the inversion. Fig. 11(a) displays the available PGVs as function of the epicentral distance compared with the adopted GMPE. The same figure also shows the residuals distribution (i.e. log of observed minus log of predicted value including VS_{30}). Fig. 11(b) displays the ratio between observed and predicted PGVs as function of the station azimuth.

In a previous study, Convertito *et al*. (2012) demonstrated that the Mach number α is correlated with the *e*-parameter. Thus, in order to reduce the correlation, we performed a set of inversions for different α-values ranging between 0.2 and 0.9 with a step of 0.1. The best value is finally selected by applying the statistical significance *t*-test on the residuals distribution at 95 per cent level of confidence. The result of the test is shown in Fig. 12(a) that, for each investigated α-value, shows the value of the statistic *t* and the corresponding *p*-value (e.g. Draper & Smith 1996). The *p*-value (ranging between 0 and 1) is the probability of obtaining the observed sample results, or more unfavourable results, when the null hypothesis is actually true. The best value is identified by a cross and corresponds to $\alpha = 0.6$. Given the best Mach number value, as described above, the corresponding *a-posteriori* pdf and relative marginal pdfs are then analysed to infer the best-model components (*L, W*, ϕ and e) and the associated uncertainties, where *L* and *W* represent the length and the width of the surface fault projection.

The best model corresponding to the maximum of the *a-posteriori* pdf is given by $\phi = 220^\circ \pm 20^\circ$, $e = 0.1 \pm 0.2$, $L = 2.7$ (1.7, 2.8) km and $W = 2.7$ (1.8, 2.8) km. Note that the upper bounds of the estimated uncertainties on *L* and *W* correspond to limit of the prior information. The preferred solution for the surface fault projection and for the horizontal rupture direction is displayed in Fig. 1. The marginal *a-posteriori* pdf on the *e*-parameter is shown in Fig. 12(b). Although the data shown in Fig. 11 appear to be scattered, the resulting model clearly indicates that, in addition to the dominant rupture direction ϕ, a secondary rupture direction is also found at $22^\circ \pm 30^\circ$. The presence of two rupture directions is also confirmed by the inferred value of the parameter *e*, which indicates that the rupture was in fact not purely unilateral. The data points larger than 2 between 20° and 40° azimuth in Fig. 11(b) could be thought as inducing the secondary rupture direction. Indeed, we verified that this latter still results even discarding the above-mentioned data.

Note that, whatever *L* and *W*, the most probable model for the surface fault projection is always characterized by $L \sim W$ (Fig. 12d). As a further check, we tried to set *L* and *W a-priori*, also choosing values outside the highest pdf area (Fig. 12d), even allowing different length and width. The general results do not change, giving

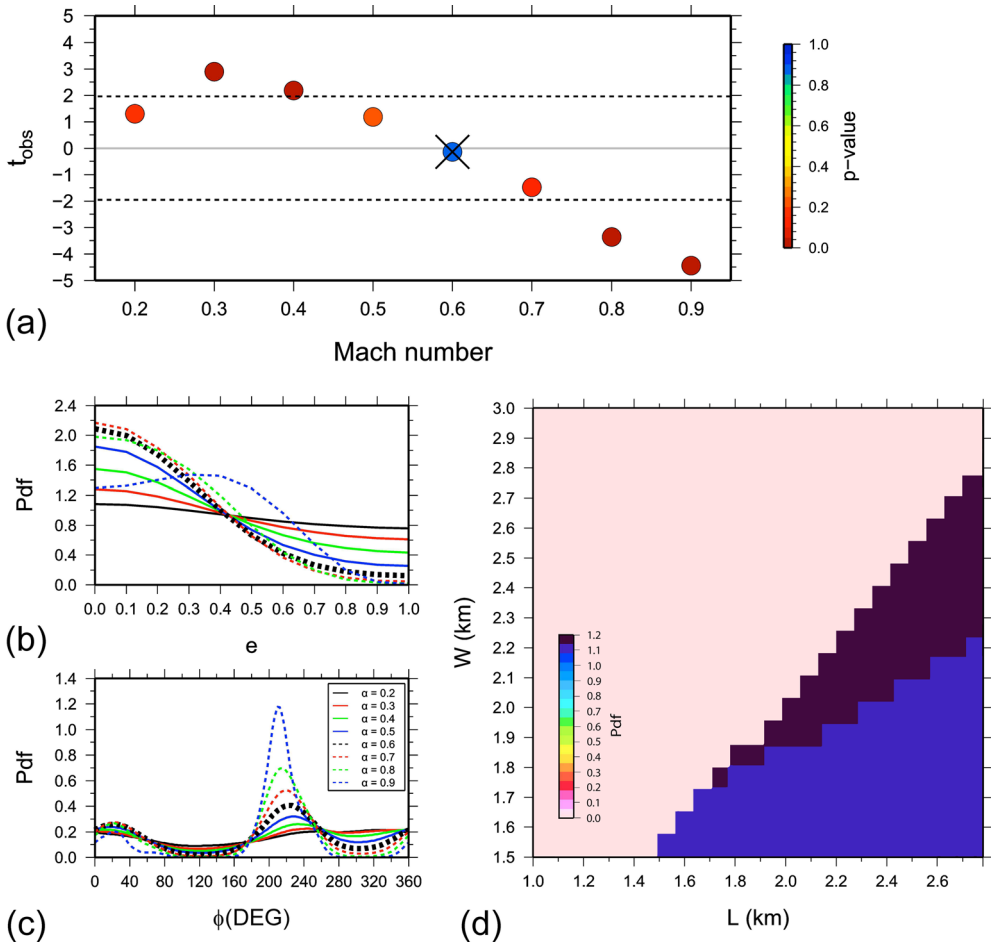

Figure 12. (a) Result of the *t*-test for each of the explored values of the Mach number α. (b) Probability density functions on e, for each α-value. (c) Marginal probability density functions versus ϕ, for each α-value, as in (b). In both (b) and (c), the bold black dashed line identifies the best α-value**.** (d) Marginal probability density functions on L and W, corresponding to the best α-value. The pdfs shown in these panels are used to estimate the uncertainty associated to the analysed parameters, whereas the best-model parameters, as reported in the text, correspond to the model maximizing the *a-posteriori* joint pdf.

similar values for ϕ, α and e. This outcome indicates that, for light to moderate earthquakes, L and W might be poorly resolved.

2.3.2 PGV^{Main}/PGV^{EGF}

The evident data scattering in Fig. 11(b) is likely to be due to the oversimplified modelling of both propagation and site effects adopted in the GMPE. In general, the more intricate the tectonic environment, like the Apennine chain, the less appropriate can be the use of 1-D GMPEs, in particular for small-to-moderate magnitude events. On the other hand, in principle, the structural complexity can be taken into account by the EGF; thus, dividing the spectral amplitude of the main shock by those of the EGF should allow a more accurate removal of the propagation + site effects. Since source directivity affects the displacement source spectrum only at frequencies around and higher than the corner frequency f_c, it is theoretically appropriate to measure the PGVs of both main shock and EGF at frequencies larger than f_c^{Main} and smaller than f_c^{EGF}. On this basis, assuming $f_c \sim 1$ Hz for a magnitude 5.0 event, we chose the same EGF used above and filtered both main shock and EGF in the range 0.8–10.0 Hz, thus in between the corner frequency of the main shock and the EGF. The upper limit is selected in order to cut-off the low signal-to-noise content in the waveforms and to minimize possible directivity effects of the EGF. Fig. 13 shows the resulting ratios at stations for which both not clipped main shock and EGF recordings were available. The PGV^{Main}/PGV^{EGF} display a significantly smoother azimuthal variability than the corresponding $PGV^{observed}/PGV^{predicted}$ values in Fig. 11(b), indicating a more reliable removal of the propagation and site effects. By using the C_d function (eq. 1), we fit the data finding a dominant rupture direction toward $\phi = 171^\circ \pm 11^\circ$, with Mach number $\alpha = 0.5 \pm 0.1$ and percent unilateral rupture $e = 0.2 \pm 0.1$ (the uncertainties correspond to the asymptotic standard errors as given by GNUPLOT; Janert 2009).

3 DISCUSSION AND CONCLUSIONS

Source directivity of large earthquakes, due to asymmetric rupture propagation, has been widely studied. The final effect of the source directivity on the observed ground motion field is to modify the amplitude and frequency content of the recorded signal as function of the station azimuth (e.g. Ben-Menahem 1961). In particular, based on the rupture velocity value, the amplitude at stations located at azimuths close to the rupture direction may be as large as 10 times than those in the opposite direction. However, observations of rupture directivity of moderate (e.g. Boatwright 2007; Seekins & Boatwright 2010) or small (e.g. Wang & Rubin 2011; Convertito & Emolo 2012; Kane *et al*. 2013) earthquakes are limited.

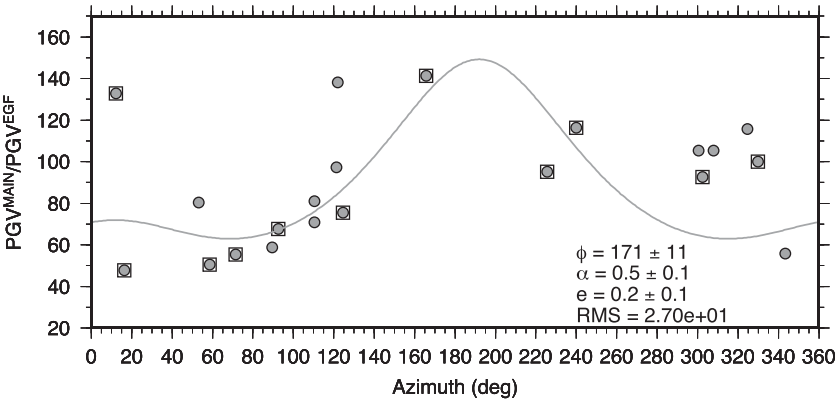

Figure 13. PGV^{MAIN}/PVG^{EGF} ratio as a function of station azimuth. Grey continuous line represents the best-fit model whose parameters are reported in the lower right corner. Squares indicate the stations at which apparent STF duration is available (Fig. 5).

Indeed, seismic data resolution and non-uniform stations azimuth coverage may hamper the identification of source directivity. Nevertheless, also for moderate earthquakes, directivity—together with site effects—can contribute to increase the damage level (e.g. Chen & Scawthorn 2003; Seekins & Boatwright 2010). This is the case of the 2013 December 29, Matese, $M_w = 5.0$, earthquake analysed in this study for which structural and non-structural damage to cultural and civil structures were documented (Convertito *et al*. 2014) and ascribed also to source effects.

In order to investigate the source directivity of the Matese earthquake, we applied six different approaches that analyse the recorded signal both in time and frequency domains. The results exposed above should be considered in the light of the assumptions behind and the limits of each method. Overall, assuming simplified source kinematics to model rupture directivity might not give precise indications on the real values of length and propagation velocity of the rupture. However, each method is able to provide with reliable indication on the dominant rupture direction, which is a fundamental requirement to estimate potential damage effects.

As for the forward modelling of STFs, its effectiveness relies mainly on the selection of a suitable EGF, not a trivial issue for a moderate event recorded at sparse seismic networks. In addition, the relatively small magnitudes may produce instability in the deconvolution operation. In these cases, the recognition of common features among the resulting STFs—a crucial element for the forward modelling—can be challenging. In the analysis of the 2013 Matese earthquake, we were able to identify source signatures that helped in determining rupture parameters. On the other hand, both forward and inverse modelling of the STFs, still providing with very coherent results, did not allow the resolution of the possible bilateral component of the fracture, as instead evidenced by the other described approaches (e.g. PGV inversion). This is likely due to a predominant unidirectional rupture patch, masking the possible secondary breakage in the moment rate functions.

Concerning the parametric spectral inversion, this method suffers from an inherent correlation between attenuation parameter Q and corner frequency f_c. This is particularly true in the case of moderate magnitude events, whose source corner frequency is within the frequency range where the effect of the anelastic attenuation on the radiated spectrum is stronger. Besides, in the case analysed above, we assumed an almost constant average, frequency independent, Q_0 factor for the investigated area. This assumption may not be effective for a complex tectonic context such as the Southern Apennines. Both these elements result in the apparent scattering of the estimated corner frequencies with the azimuth, relative to the model (Fig. 10). In spite of these limitations, the dominant rupture direction inferred from the f_c inversion is consistent with those resulting from the STF analysis.

Unlike techniques based on STF modelling and f_c analysis, inferring source directivity from PGVs inversion relies on directly measurable data, which usually are also much more abundant and can be analysed straightforwardly. However, the simplified isotropic attenuation model used in the GMPE to account for geometrical spreading and anelastic attenuation is less effective than the attenuation model used for retrieving f_c and originates the evident scattering of the PGVs as a function of the azimuth. Moreover, accounting for site effect by using specific coefficients in the GMPE, depending on the VS_{30} value at each station, provides only a first-order correction that cannot significantly reduce the scattering.

Methods that do not depend on assumptions on the velocity model, such as EGF, represent well-established techniques for reliable recognition of the STF. In the analysis described above, we demonstrate that, even in the case of punctual measurements such as PGV, the ratio PGV^{Main}/PGV^{EGF} can be effective in the separation of source effects as rupture directivity, as long as a suitable EGF is available.

Notably, the STF forward modelling and all the techniques adopted to invert the C_d function (eq. 1), using different data, agree in identifying a dominant rupture direction toward S-SW for the 2013 December 29, Matese, $M_w = 5.0$ earthquake, with most solutions ranging between 170° and 190° (Table 1). Incidentally, we note that this outcome agrees with both the observed macroseismic intensity distribution, evidencing higher values southwest of the epicentre (Convertito *et al*. 2014), and the felt reports (http://www.haisentitoilterremoto.it/, last accessed 2015 July 7), indicating higher intensities southward.

Since the aftershock double-difference location (Di Luccio *et al*. in preparation) identifies the SW-dipping as the rupture plane (Fig. 1), the above result corresponds to oblique-downdip rupture propagation. This is in agreement with the location of the aftershocks relative to the main shock, depicting an area elongated S-SE, with some events located obliquely downdip with respect to the main shock, in spite of its relatively large hypocentral depth. We emphasize that downdip rupture propagation is generally not so common (Mai *et al*. 2005), thus representing interesting case studies. Besides, due to limited extent of the rupture, the directivity effect resulting from our investigation, we can reasonably exclude that this arises from the excitation of sources at different

Table 1. Best rupture (dominant ϕ_1 and secondary ϕ_2) directions, surface projection of rupture length (L) and width (W), percent unilateral rupture value (e) and rupture velocity v_r or S-wave Mach number α, as inferred from the analysis of the time- and frequency-domain data **(**STFMOD: Source Time Function Forward Modelling; STFDUR: Apparent STF Duration inversion; STFINV1: Source Time Inversion, single-line source; STFINV2: Source Time Inversion, two-line source**;** SPECTINV: Spectral Inversion; PGVINV: PGV Inversion; PGVM/E: PGV^{MAIN}/PGV^{EGF} ratio inversion).

Approach	ϕ_1 (°)	ϕ_2 (°)	L (km)*	W (km)*	e	v_r (km s^{-1}) or α
STFMOD	180 ± 30	–	1.7 ± 0.2	–	–	1.55 ± 0.23 km s^{-1}
STFDUR	188 ± 29	–	–	–	–	0.62 ± 0.02 km s^{-1}
STFINV2	130 (127, 132)	250 (245, 255)	3.00†	3.00†	–	1.8 (1.7, 2.0) km s^{-1}
STFINV1	185 (172, 198)	–	1.85†	3.00†	–	1.8 (1.6, 1.9) km s^{-1}
SPECTINV	169 ± 7	–	–	–	0.0 ± 0.1	0.5 ± 0.1††
PGVINV	214 ± 27	25 ± 30	2.7 (1.7, 2.8)	2.7 (1.8, 2, 8)	0.1 ± 0.2	0.6††
PGVM/E	171 ± 11	–	–	–	0.2 ± 0.1	0.5 ± 0.1††

*Surface projection.
†Assumed (as for W, the value is only used to constrain M_0).
††Mach number $\boldsymbol{\alpha}$.

depth—characterized by distinct wave velocities—as possible, in principle, for large events (Cesca *et al*. 2011).

Recalling that our modelling assumes a linear horizontal source, representing the surface projection of the actual rupture, the downdip propagation of the fracture explains the estimated relatively short rupture length and low rupture velocity. For the given fault, dipping 41° toward N215°, the actual rupture length and velocity is expected to be larger. Thus, the fracture duration of $\tau = 1.1$ s and surface projection of the rupture velocity $v_{rh} = 1.55$ km s^{-1}, as resulting from the STF analysis (Section 2.1.1), corresponds to $v_r = 1.9$ km s^{-1} and rupture length $L = 2.1$ km on the fault plane. In this framework, the secondary rupture direction approximately northward oriented, identified by both the f_c and PGV inversions, corresponds to an updip rupture propagation of a minor patch, in agreement with the high f_c and PGV observed at station located north of the epicentre, at short distances (Figs 10 and 11).

In conclusion, even in the case of moderate magnitude events with not prominent directivity effects, different techniques, based on distinct data, converge in giving consistent results on rupture direction. However, since the adopted methods analyse data that are sensitive to different characteristics of the ground motion, each of them contributes with pieces of information that converge toward a more reliable image of the source rupture. Thus, the main conclusion of this study is that the directivity of small-to-moderate earthquakes should be always investigated by comparing the results of several distinct analyses.

ACKNOWLEDGEMENTS

We thank F. Gallovič and S. Cesca for their careful reviews. All plots were produced using Generic Mapping Tools (Wessel & Smith 1991).

REFERENCES

Akaike, H., 1974. A new look at the statistical model identification, *IEEE Trans. Automat. Control,* **19**(6), 716–723.

Aki, K. & Richards, P., 1980. *Quantitative Seismology: Theory and Methods,* W. H. Freeman.

Ameri, G., Gallovič, F. & Pacor, F., 2012. Complexity of the M_w 6.3 2009 L'Aquila (central Italy) earthquake: 2. Broadband strong motion modeling, *J. geophys. Res.,* **117,** B04308, doi:10.1029/2011JB008729.

Aster, R.C., Borchers, B. & Thurber, C.H., 2005. *Parameter Estimation and Inverse Problems,* Elsevier Academic Press.

Ben-Menahem, A., 1961. Radiation of seismic surface waves from finite moving sources, *Bull. seism. Soc. Am.,* **51**(3), 401–435.

Ben-Menahem, A. & Singh, S.J., 1981. *Seismic Waves and Sources,* Springer-Verlag.

Bernard, P., Herrero, A. & Berge, C., 1996. Modelling directivity of heterogeneous earthquake ruptures, *Bull. seism. Soc. Am.,* **86**(4), 1149–1160.

Bianco, F., Del Pezzo, E., Castellano, M., Ibanez, J.M. & Di Luccio, F., 2002. Separation of intrinsic and scattering seismic attenuation in the southern Apennine zone, Italy, *Geophys. J. Int.,* **150**(1), 10–22.

Bindi, D., Pacor, F., Luzi, L., Puglia, R., Massa, M., Ameri, G. & Paolucci, R., 2011. Ground motion prediction equations derived from the Italian strong motion data base, *Bull. Earth. Eng.,* **9**(6), 1899–1920.

Boatwright, J., 1980. A spectral theory for circular seismic sources; simple estimates of source dimension, dynamic stress drop, and radiated seismic energy, *Bull. seism. Soc. Am.,* **70**(7), 1–27.

Boatwright, J., 2007. The persistence of directivity in small earthquakes, *Bull. seism. Soc. Am.,* **97**(6), 1850–1861.

Bouchon, M., Toksöz, N., Karabulut, H., Bouin, M.P., Dietrich, M., Aktar, M. & Edie, M., 2002. Space and time evolution of rupture and faulting during the 1999 Izmit (Turkey) earthquake, *Bull. seism. Soc. Am.,* **92**(1), 256–266.

Brune, J.N., 1970. Tectonic stress and the spectra of seismic shear waves from earthquakes, *J. geophys. Res.,* **75**(26), 4997–5009.

Cesca, S., Heimann, S. & Dahm, T., 2011. Rapid directivity detection by azimuthal amplitude spectra inversion, *J. Seismol.,* **15**(1), 147–164.

Chen, W.F. & Scawthorn, C., 2003. *Earthquake Engineering Handbook,* CRC Press.

Convertito, V., Caccavale, M., De Matteis, R., Emolo, A., Wald, D. & Zollo, A., 2012. Fault extent estimation for near-real-time ground-shaking map computation purposes, *Bull. seism. Soc. Am.,* **102**(2), 661–679.

Convertito, V. & Emolo, A., 2012. Investigating rupture direction for three 2012 moderate earthquakes in northern italy from inversion of peak-ground motion parameters, *Bull. seism. Soc. Am.,* **102**(6), 2764–2770.

Convertito, V. & Pino, N.A., 2014. Discriminating among distinct source models of the 1908 Messina Straits earthquake by modelling intensity data through full wavefield seismograms, *Geophys. J. Int.,* **198**(1), 164–173.

Convertito, V., Catalli, F. & Emolo, A., 2013. Combining stress transfer and source directivity: the case of the 2012 Emilia seismic sequence, *Sci. Rep.,* **3,** 3114, doi:10.1038/srep03114.

Convertito, V., Cubellis, E., Marturano, A., Obrizzo, F. & Petrazzuoli, S.M., 2014. Terremoto del Matese (M_w = 5.0), Indagine speditiva degli effetti nell'area epicentrale e analisi preliminare della sequenza sismica, *Rapporti Tecnici INGV,* 290, ISSN 2039-7941.

Courboulex, F., Dujardin, A., Vallée, M., Delouis, B., Sira, C., Deschamps, A., Honore, L. & Thouvenot, F., 2013. High-frequency directivity effect for an M_w 4.1 earthquake, widely felt by the population in southeastern France, *Bull. seism. Soc. Am.,* **103**(6), 3347–3353.

Di Luccio, F. & Pino, N.A., 2011. Elementary seismological analysis applied to the 6 April 2009 L'Aquila mainshock and its larger aftershock, *Boll. Geofis. Teor. Appl.,* **52**(3), 389–406.

DISS Working Group, 2010. *Database of Individual Seismogenic Sources (DISS), Version 3.1.1: A Compilation of Potential Sources for Earthquakes Larger Than M 5.5 in Italy and Surrounding Areas,* © INGV 2010—Istituto Nazionale di Geofisica e Vulcanologia, doi:10.6092/INGV.IT-DISS3.1.1. Available at: http://diss.rm.ingv.it/diss/, last accessed 20 September 2016.

Draper, N.R. & Smith, H., 1996. *Applied Regression Analysis,* 3rd edn, John Wiley & Sons Inc.

Dreger, D.S., Huang, M.-H., Rodgers, A., Taira, T. & Wooddell, K., 2015. Kinematic finite-source model for the August 24, 2014 South Napa, CA earthquake from joint inversion of seismic, GPS and InSAR Data, *Seismol. Res. Lett.,* **86**(2), 327–334.

Ferranti, L., Milano, G., Burrato, P., Palano, M. & Cannavo, F., 2015. The seismogenic structure of the 2013–2014 Matese seismic sequence, Southern Italy: implication for the geometry of the Apennines active extensional belt, *Geophys. J. Int.,* **201**(2), 823–837.

Gomberg, J. & Bodin, P., 1994. Triggering of the Little Skull Mountain, Nevada earthquake with dynamic strains, *Bull. seism. Soc. Am.,* **84**(3), 844–853.

Gomberg, J., Bodin, P. & Reasenberg, P.A., 2003. Observing earthquakes triggered in the near field by dynamic deformations, *Bull. seism. Soc. Am.,* **93**(1), 118–138.

Holden, C., 2011. Kinematic source model of the 22 February 2011 M_w 6.2 Christchurch earthquake using strong motion data, *Seismol. Res. Lett.,* **82**(6), 783–788.

Janert, K.P., 2009. *GNUPLOT in Action: Understanding Data With Graphs,* Manning Publications Co.

Joyner, W.B., 1991. Directivity for non-uniform ruptures, *Bull. seism. Soc. Am.,* **81**(4), 1391–1395.

Joyner, W.B. & Boore, D.M., 1981. Peak horizontal acceleration and velocity from strong-motion records including records from the 1979 Imperial Valley, California, earthquake, *Bull. seism. Soc. Am.,* **71**(6), 2011–2038.

Kanamori, H. & Brodsky, E.E., 2004. The physics of earthquakes, *Rep. Prog. Phys.,* **67,** 1429–1496.

Kane, D.L., Shearer, P., Goertz-Allmann, B.P. & Vernon, F., 2013. Rupture directivity of small earthquakes at Parfield, *J. geophys. Res.,* **118,** 212–221.

López-Comino, J.-Á., Mancilla, F., Morales, J. & Stich, D., 2012. Rupture directivity of the 2011, M_w 5.2 Lorca earthquake (Spain), *Geophys. Res. Lett.,* **39,** L03301, doi:10.1029/2011GL050498.

Mai, P.M., Spudich, P. & Boatwright, J., 2005. Hypocenter locations in finite-source rupture models, *Bull. seism. Soc. Am.,* **95**(3), 365–980.

Marquardt, D., 1963. An algorithm for least-Squares estimation of nonlinear parameters, *SIAM J. Applied Math,* **11**(2), 431–441.

McGuire, J.J., 2004. Estimating finite source properties of small earthquake ruptures, *Bull. seism. Soc. Am.,* **94**(2), 377–393.

Michelini, A., Faenza, L., Lauciani, V. & Malagnini, L., 2008. ShakeMap implementation in Italy, *Seismol. Res. Lett.,* **79**(5), 688–697.

Milano, G., Di Giovambattista, R. & Ventura, G., 2005. The 2001 seismic activity near Isernia (Italy): implications for the seismotectonics of the Central–Southern Apennines, *Tectonophysics,* **401**(3–4), 167–178.

Nelder, J.A. & Mead, R., 1965. A simplex method for function minimization, *Comput. J.,* **7**(4), 308–313.

Pacor, F. *et al.*, 2016a. Spectral models for ground motion prediction in the L'Aquila region (central Italy): evidence for stress-drop dependence on magnitude and depth, *Geophys. J. Int.* **204**(2), 697–718.

Pacor, F., Gallovič, F., Puglia, R., Luzi, L. & D'Amico, M., 2016b. Diminishing high-frequency directivity due to a source effect: empirical evidence from small earthquakes in the Abruzzo region, Italy, *Geophys. Res. Lett.,* **43**(10), 5000–5008.

Parolai, S., Bindi, D., Baumbach, M., Grosser, H., Milkereit, C., Karakisa, S. & Zünbül, S., 2004. Comparison of different site response estimation techniques using aftershocks of 1999 Izmit earthquake, *Bull. seism. Soc. Am.,* **94**(3), 1096–1108.

Pawitan, Y., 2013. *In All Likelihood: Statistical Model and Inference using Likelihood,* Oxford Univ. Press.

Pino, N.A., Giardini, D. & Boschi, E., 2000. The 1908 December 28 Messina Straits (southern Italy) earthquake: waveform modeling of regional seismograms, *J. geophys. Res.,* **105**(11), 25 473–25 492.

Pino, N.A. & Mazza, S., 2000. The Umbria-Marche (central Italy) earthquakes: relation between rupture directivity and sequence evolution for the $M_w > 5$ shocks, *J. Seismol.,* **4**(4), 451–461.

Pino, N.A., Palombo, B., Ventura, G., Perniola, B. & Ferrari, G., 2008. Waveform modeling of historical seismograms of the 1930 Irpinia earthquake provides insight on "blind" faulting in Southern Apennines (Italy), *J. geophys. Res.,* **113,** B05303, doi:10.1029/2007JB005211.

Seekins, L.C. & Boatwright, J., 2010. Rupture directivity of moderate earthquakes in Northern California, *Bull. seism. Soc. Am.,* **100**(3), 1107–1119.

Somerville, P.G. *et al.*, 1999. Characterizing crustal earthquake slip models for the prediction of strong ground motion, *Seismol. Res. Lett.,* **70,** 59–80.

Sonley, E. & Abercrombie, R.E., 2006. Effects of methods of attenuation correction on source parameter determination, in *Earthquakes: Radiated Energy and the Physics of Faulting*, Vol. 170, pp. 91–97, eds Abercrombie, R. *et al.*, Geophys. Monogr. Ser., AGU.

van der Elst, N.J. & Brodsky, E.E., 2010. Connecting near-field and far-field earthquake triggering to dynamic strain, *J. geophys. Res.,* **115,** B07311, doi:10.1029/2009JB006681.

Wald, D.J., Heaton, T.H. & Hudnut, K., 1996. The slip history of the 1994 Northridge, California, earthquake determined from strong motion, teleseismic, GPS and leveling data, *Bull. seism. Soc. Am.,* **86**(1B), S49–S70.

Wang, E. & Rubin, A.M., 2011. Rupture directivity of microearthquakes on the San Andreas Fault from spectral ratio inversion, *Geophys. J. Int.,* **186**(2), 852–866.

Wells, D.L. & Coppersmith, K.J., 1994. New empirical relationships among magnitude, rupture length, rupture width, rupture area, and surface displacement, *Bull. seism. Soc. Am.,* **84**(4), 974–1002.

Wessel, P. & Smith, W.H.F., 1991. Free software helps map and display data, *EOS, Trans. Am. geophys. Un.,* **72**(41), 441–446.

Zollo, A., Orefice, A. & Convertito, V., 2014. Source parameter scaling and radiation efficiency of microearthquakes along the Irpinia fault zone in southern Apennines, Italy, *J. geophys. Res.,* **119**(4), 3256–3275.